Lead (Pb^{2+}) Ion Sensor Development using Optical Fiber Gratings and Nanocomposite Materials

Souvik Ghosh[*1,4], Kasun Dissanayake[2], S. Asokan[3], T. Sun[1], B. M. Azizur Rahman[1] and Kenneth T. V. Grattan[1]

[1]*Institute of Sensors and Instrumentation, City, University of London, London, EC1V 0HB, UK*

[2]*Sri Lanka Institute of Nanotechnology Pvt. Ltd., Sri Lanka*

[3]*Indian Institute of Science, Bangalore, India*

[4]*Now moved to University College London, London WC1E 6BT, UK*

*Corresponding Author, souvik.ghosh.1@city.ac.uk

Tel: +44-7405137454

Keywords

Long period grating, Fiber Bragg grating, Heavy metal ion sensor, Temperature sensor, Chemical sensor, Artificial Neural Network, graphene oxide, polymer

Abstract

Research on compact, flexible optical sensors for water quality monitoring, specifically targeting heavy metal ion monitoring, has become extremely important due to the increasing number of water pollution incidents seen worldwide where such heavy metals are involved. Optical fiber-based sensors provide an excellent basis for creating new sensing solutions across a wide area, including for energy, healthcare, structural monitoring, defense and importantly here for environmental monitoring. An innovative, cost-optimized sensor solution to better heavy metal detection is proposed, by introducing a hybrid optical fiber grating sensor system based on concatenating a Long Period Grating (LPG) and Fiber Bragg Grating (FBG) for the concurrent detection of an important, specific heavy metal ion pollutant (in this case lead (Pb^{2+})). The approach uses the functionalization of an optical fiber grating with a chemically synthesized novel nanocomposite material (together with temperature sensing to allow such corrections to be applied). Such a method not only significantly enhances the system sensitivity (achieving 2.547

nm/nM), with a detection limit (0.5 nM), and high selectivity to the Pb^{2+} ions, but also mitigates the shortcomings of cross-sensitivity seen with many such sensors. Furthermore, in this work, the incorporation of a forward Artificial Neural Network (ANN)-based predictive algorithm has been incorporated to create an effective, well-calibrated system whose characteristics as an intelligent, highly sensitive system has been demonstrated in the detection of the sub-nanomolar concentration of Pb^{2+} ion in drinking water.

1. Introduction

1.1 The problem of heavy metal pollution

In 2015, the United Nations (UN) highlighted seventeen 'Sustainable Development Goals' out of which the 6^{th} and 14^{th} goals emphasized the necessity of 'Clean water and sanitization' and 'Life below water', respectively, for a better quality of life [1]. Moreover, the World Health Organization (WHO) has quantified the standards of heavy metal contamination in potable water in their guidelines [2], which have emphasized the global importance of water quality monitoring and the requirement of cost-optimized, compact, and flexible water monitoring platforms to do so. In this work, such a system designed around the Internet of Things (IoT)-based principles and suitable for remote interrogation, has been proposed and its performance discussed when used to address heavy metal contamination in water.

Out of 35 naturally occurring metals, 23 are considered as heavy metals because of their intrinsic properties of high atomic weight, density, and tensile strength [3, 4]. Unfortunately, long-term exposure to even moderate amounts of such contaminants can lead to severe health issues for humans and animals, because of their acute toxicity. Amongst these, lead (Pb), arsenic (As), cadmium (Cd), mercury (Hg), and chromium (Cr) are the most commonly seen as pollutants in water – lethal for living organisms even in small quantities. A further unfortunate problem is that these materials accumulate in the environment – they are non-biodegradable, and the extended half-life of heavy metals makes them prone to accumulate in soft tissues and organs. Even at picomolar concentration level, lead ions can substitute the calcium ions in tissue and thus affect the protein kinesis – some excellent work by Jaishankar *et al.* and Flora *et al*. has recently reviewed heavy metal toxicities and intoxication mechanisms, [4, 5].

The focus in this work is on lead (Pb) as, among the group of heavy metals mentioned above, lead causes chronic toxicity yet is still widely used in many parts of the developing world in manufacturing, paints, ammunition, solder, pipes and the battery industry, for example. Often in such places, the natural leaching process and continuous outflow of poorly treated industrial effluent cause lead pollution in the aquatic environment (despite legislation to prevent it), where lead is commonly found in the ionic state in water or the environment, as it has a strong ability to replace the regular monovalent and bivalent cations.

1.2 Sensing approaches for in-situ heavy metal detection

Conventional detection technology, such as using inductively-coupled plasma mass spectrometry (ICP-MS), atomic absorption and fluorescence spectrometry and electrochemical analysis, while effective and seen as the laboratory 'gold standard' typically involves the use of expensive instruments, long detection times and complicated sample preprocessing; while high maintenance, above all the major drawback, is not being well suited to real-time, on-site detection due to laboratory use requiring samples to be brought there for analysis. In order to overcome the problem and fill the technological gap to allow simpler, *in situ* analysis to be carried out (where sampling is not required), recent research on fibre-optic [6, 7] sensors offer promise as an effective alternative approach for implementation outside the laboratory environment. The intrinsic characteristics offered, such as flexibility, compactness, immunity to electromagnetic interference, and potentially good species selectivity from such technology has made optical fiber-based systems well suited to an on-site approach (preferable for real-time remote monitoring of key toxic pollutants including heavy metals, as well as hormones, pesticides, and pharmaceutical residues in water). The researchers reported in the literature, several different optical fiber-based probe configurations, e.g., fibers with Bragg gratings written in [8, 9], etched fiber Bragg gratings [10], in-line interferometers [11], microfibers [12], U-bend fibers [13], the use of whispering gallery modes [14], long-range surface plasmon resonance (LSPR) sensors [15, 16], fiber fluorometers [17], and modal interferometers in microstructured optical fibers [18] that have been developed and investigated for a variety of sensing applications. Amongst these, multiple promising approaches for metal ion sensing have been discussed, for example, an in-line fiber interferometer [19], tapered microfibers [20], optical fiber absorbance [21] and fluorescence monitoring [22], hybrid electrochemical-fiber sensors [23], as well as grating-based [24] and plasmonic sensors [25,

26] as compact and cost-effective heavy metal ion detectors. However, further research is needed to improve their performance for better use outside the laboratory, for example, to enhance the sensitivity and functionality of such systems to create the new and better sensors that in-the-field use requires.

1.3 An optical fiber LPG and FBG-based sensor

This work reports new research, based on the development of a chemically functionalized hybrid grating-based fiber-optic heavy metal ion sensor by incorporating both a higher-order Long Period Grating (LPG) and a Fiber Bragg Grating (FBG), written within the fiber as the basis of new and better sensor systems. Here, the attenuation bands of both the LPG and FBG used were optimized to fit within the familiar optical S-band, around which wavelengths a system for selective sub-nanomolar detection both of Pb^{2+} ion and ambient temperature was developed. The FBG used is familiar as a temperature and strain sensor, but it does not have an evanescent field outside the cladding, making it less suitable for surface sensing unless etched or tapered – a process that makes the fiber structurally weaker and fragile. Thus, in this approach, the FBG attenuation band is simultaneously used for water temperature sensing and as a reference point for accurate measurements of the relative wavelength shift of an LPG also written into the fiber ($\Delta\lambda_R$). The mode coupling between the core and co-propagating cladding modes with strong evanescent fields make such an LPG an efficient device for external surface sensing both in transmission [27 – 30] and reflection modes [31, 32]. Doing so does not affect the structural integrity of the fiber, unlike other sensor designs which do, requiring chemical etching [33], tapering [34], and structurally mismatched multiple splicing points [35] and is an advantage of the approach taken here.

2. Sensor Design and Fabrication

The design and fabrication of the sensor can be summarized as follows. In order to make the fiber grating sensor selective to Pb^{2+} and to minimize cross-sensitivity, the sensor was based around an optical fiber functionalized with a multilayer coating of ammonia-doped graphene oxide and cross-linked chitosan-based nanocomposite material and poly-(acrylic acid) (PAA) polymer. The nanocomposite used had been designed specifically to provide ample chelating sites for the adsorption of Pb^{2+} ions. Moreover, the multilayer deposition of fiber surface was used to enhance

the evanescent field strength, with the aim being for a small refractometric variation due to metal ion adsorption to be promptly detected. Simultaneously, to enhance the signal analysis, a forward artificial neural network (ANN) [36 – 38] was developed and then trained to predict the sensor characteristics, dealing with the nonlinear response for effective detection of Pb^{2+} ions in water. The details of the optical and sensor coating design, fabrication and evaluation are discussed in the subsequent sections.

2.1 *Fiber optic multi-grating sensor design*

A fiber optic grating-based sensor approach for the simultaneous detection of the sub-nanomolar concentration of a toxic heavy metal ion (specifically lead (Pb^{2+}) in this case) – as well as the ambient temperature, recognizing that correction data will be needed – is proposed. Figure 1(a) shows a schematic of the fiber optic hybrid grating sensor design, in which both an LPG and a FBG [39] were written along a single-mode fiber – the inset shows the experimentally-obtained transmission spectra from their combined spectral response, with the narrow peak being due to the FBG and the broader peak coming from the LPG. The FBG also provides a known wavelength calibration, against which the much greater spectral shift of the LPG can be measured. A LS-1 series broadband source (360 – 2000 nm – from Ocean Optics) was used together with a Yokogawa AQ6370C Optical Spectrum Analyzer (OSA).

The coated LPG was the sensor element for Pb^{2+} detection and Fig. 1(b) shows a schematic diagram of its working principle, where the periodic refractive index variation in the LPG used provides efficient coupling of the fiber core mode ($LP_{0,1}$) to the (simultaneously) propagating cladding modes ($LP_{0,m}$ where $m = 2, 3, 4, \ldots$) at a number of distinct resonant wavelengths ($\lambda_{0,m}^{LPG}$). The core-clad mode couplings and their resonance wavelengths are governed by the phase-matching condition, $\left\{n_{eff}^{0,1}(\lambda_{op}) - n_{eff}^{0,m}(\lambda_{op})\right\} \cdot \Lambda = \lambda_{0,m}^{LPG}$, where $n_{eff}^{0,1}$ and $n_{eff}^{0,m}$ represent the effective indices of the core and m^{th} order cladding mode, respectively, where Λ denotes the grating period.

An in-house laser-based fiber grating inscription facility [40, 41] was used to manufacture both the LPGs and FBGs, writing these into boron-doped photosensitive silica-clad single-mode fiber (PS1250/1500 from Fibercore, UK). LPGs and FBGs of 30 mm and 10.16 mm length, respectively,

were inscribed into the fiber core by using a deep-UV KrF excimer laser operating at 248 nm with a pulse energy of 10 mJ and frequency of 100 Hz. In the case of the LPG, a periodic refractive index modulation with a period of 250 μm was generated in the fiber core using a custom-made metal amplitude mask to obtain the attenuation peak (Peak-1) of $LP_{0,9}$ mode within the S-band region.

2.2 Theoretical background

The coupled-mode theory has been employed to understand and thus optimize the behaviors of LPG modes and their attenuation bands (the optical fiber and gratings specifications, used for the simulation and experiment, are given in Table S1). Figure 2(a) shows the effective index (n_{eff}) dispersion plot of the fiber core (m = 1) and cladding modes (m = 2, 3, 4…), illustrating that the n_{eff} values of the core and clad modes decrease and approach the core and clad refractive indices, respectively, with increasing operating wavelength (λ_{op}). It is evident that a higher-order clad mode, which will have a greater attenuation, will show a higher modal loss. For sensing applications, tracking the highest attenuation band provides higher sensitivity to the surrounding index change. In Fig. 2(a), although the calculated distribution of n_{eff} over the wavelength range from 1 to 2.5 μm is shown, it is convenient that the operating region is limited to 1700 nm, this being determined by the upper wavelength limit of the OSA used, and thus the LPG attenuation band of the $LP_{0,9}$ mode within the S-band (1460 – 1530 nm) was chosen for the sensor.

It is clear that at the perfect phase-matching condition, the wavelength difference ($\delta\lambda$) form of the LPG characteristic equation will be zero, as shown below.

$$\delta\lambda = \left\{n_{eff}^{0,1}\left(\lambda_{op}\right) - n_{eff}^{0,m}\left(\lambda_{op}\right)\right\} \cdot \Lambda - \lambda_{0,m}^{LPG} = 0 \qquad (1)$$

In Fig. 2(b), the $\delta\lambda$ distribution of different attenuation bands for the different cladding modes (m = 2, 3, 4, …) has been plotted over a mode number-wavelength space. The zero-marked black dashed line indicates the positions where $\delta\lambda = 0$ for different wavelengths. The $LP_{0,9}$ mode is represented by a horizontal yellow dashed-dotted line, intersecting the $\delta\lambda = 0$ curve twice. This double zero-crossing represents the dual-resonance nature of the $LP_{0,9}$ mode. It can be seen from the figure that the dual attenuation bands were situated far apart, and therefore simultaneous

interrogation of both peaks was not convenient (with the present setup). Taking advantage of the operating region of the OSA (700 – 1700 nm), the first attenuation band (peak-1) was chosen as the basis of the Pb^{2+} sensor. The FBG peak [36] was then utilized for both water *temperature* detection and a reference for the LPG spectral interrogation (as it is unresponsive to surrounding refractive index change).

The LPG which was fabricated as discussed above was simulated using OptiGrating software [42]. The spectral response of both the simulated and fabricated LPG showed an excellent agreement, as shown in Fig. S1. The FBG was written at 1524 nm, with the same laser, using a phase mask with a period of 1053 nm and both the LPG and FBG were annealed at 80^{o} C for 4 hours to stabilize their properties prior to sensor use.

2.3 Materials

All analytical grade chemicals were used, such as low molecular weight chitosan (CS), 1 mg/mL aqueous dispersion of ammonia functionalized graphene oxide ($C_mH_nO_xN_y$), 35 wt% aqueous dispersion of poly (acrylic acid) (PAA), sodium hydroxide (NaOH), EDTA, lead nitrate ($Pb(NO_3)_2$) salt, and acetone were purchased from Sigma-Aldrich, UK. Hydrochloride acid, acetic acid, ethanol, isopropanol, and deionized (DI) water were purchased from Thermo Fisher Scientific Inc., UK. 25 wt% aqueous solution of glutaraldehyde ($OHC(CH_2)_3$) was purchased from Alfa Aesear, UK. Throughout the experiment, the chemicals were used as received without any modification and purifications and all aqueous solutions were prepared with deionized (DI) water.

2.4 ***Nanocomposite material synthesis and deposition***

Cross-linked chitosan and the nitrogen-doped graphene oxide-based nanocomposite material (CCS-NGO) were prepared in the laboratory with analytical grade chemicals. First, 50 mL of 2% (w/v) acetic acid (CH_3COOH) dispersed chitosan (CS) solution was prepared by adding 1 g of CS to a 4% (v/v) CH_3COOH solution and mechanically stirred for 24 h at room temperature until the CS powder dissolves completely. Cross-linked CS (CCS) was obtained by adding 50 μl glutaraldehyde (GA) of concentration 0.1 mg/mL to a freshly prepared 2% CS solution and stirring for 10 minutes. A yellowish translucent CCS solution was obtained and stored in a conical flask, as shown in Fig. 3(a, 1). Next, the CCS-NGO nanocomposite was synthesized by adding 3 mL

water-dispersed NGO solution of concentration 1 mg/mL to the CCS solution and continuously stirred for 1 h at room temperature. Following mechanical stirring, the mixture was further sonicated for 10 minutes and finally, a dark-brown homogeneous CCS-NGO gel-like liquid was obtained. Fig. 3(a, 2) shows the image of NGO flakes, and a chemical structure of NGO is shown in Fig. 3(a, 3), where the resultant key functional groups that appeared due to ammonia functionalization are highlighted with different colors. As described by Baldovino *et al.* [43], amide (green), pyrrolic N (purple), imides, and pyridinic N (yellow) were formed due to the reaction of ammonia (NH_3) and carboxyl group, and aromatic amines (red and blue) were formed due to the reaction of NH_3, and epoxy and hydroxyl groups.

The LPG-based label-free heavy metal ion sensor was developed through a surface modification of the LPG region with a multilayer coating of CCS-NGO and PAA. A schematic diagram of a step-by-step LPG surface modification process is shown in Figs. 3(b, 1 – 3). A layer-by-layer (LbL) electrostatic adsorption process was followed for the fiber surface functionalization treatment. The LPG section was immersed in the CCS-NGO solution for 10 minutes and then lifted out carefully and dried for 5 minutes. At this stage, the cationic CCS-NGO was attached to the negatively charged fiber surface and formed a thin overlay. The negatively charged fiber surface required was obtained by soaking a clean fiber surface in a 4% (w/v) NaOH solution for 90 minutes at room temperature to activate the silanol (Si-OH) groups. Following this alkaline treatment, the fiber was consecutively washed with ethanol and DI water to eliminate alkaline residue and dried under a flow of argon gas. Besides electrostatic adsorption, the gel-like texture of CCS-NGO also helped in the formation of an ultra-thin layer. Then, the fiber was immersed in an 8% (v/v) transparent PAA solution for 10 minutes and lifted out and dried. It formed an anionic PAA layer on a positively charged CCS-NGO overlay. This completes a cycle of a $(CCS\text{-}NGO/PAA)_1$ deposition on the LPG section. It is well known that the LPG sensitivity can be modulated with the coating thickness [27, 44], thereby, an optimized coating thickness for the LPG sensor was obtained by repeating the aforementioned steps. Figure 3(c) shows an illustration of a multilayered coated fiber cross-section.

CS, NGO, and PAA are the key ingredients of the nanocomposite, and their molecular structures are shown in Fig. 3(a). The CS is a linear cationic amino-polysaccharide hydrophilic bio-sorbent with highly reactive amino ($-NH_2$) and hydroxyl (-OH) content that leads to the use CS and its

modified versions for successive heavy metal ion detection and removal [45]. In cross-linked CS, an optimized amount of GA was used to form the chitosan polymeric chains which helped to enhance its stability to form a three-dimensional network without affecting its inherent metal adsorption ability [46, 47]. The element analysis of the NGO showed that the water dispersed NGO was a composition of 47.63% carbon (C), 5.31% nitrogen (N), 3.10% sulfur (S), 41.09% oxygen (O), and 2.86% hydrogen (H) by weight. The synthesized CCS-NGO nanocomposite had a resultant characteristic from both CCS and NGO, thus enriched with the major functional groups such as amide I (NH-CO), amino ($-NH_2$), alkoxy (-OH), carboxyl (-COOH) and thiol (-SH) that are expected to play in selective adsorption of Pb^{2+} ions.

2.5 LPG modelling and simulation

Owing to the excellent light-guiding features of the LPG used, it can be a more effective and efficient basis of a chemical sensor (for example as compared to a more fragile etched-FBG [48]), while its sensing performance can be greatly enhanced by modulating the thickness and optical properties of the externally deposited sensing layer (see recent work in the literature [27, 29, 44, 49]).

For a better understanding and thus performance optimization of the LPG-based sensor, an OptiGrating [42] model of a coated LPG surrounded by water (n_{water} = 1.315) was developed to maximize the wavelength shift ($\Delta\lambda_{0,9}$) of the $LP_{0,9}$ attenuation band depending on sensing layer thickness (T_{lyr}) and refractive index (RI_{lyr}). A wide range of values of T_{lyr} (100 nm – 800 nm) and RI_{lyr} (1.31 – 1.72) were considered in the simulations carried out, and the results are shown in Fig. 4. It can be noticed that for different values of T_{lyr}, the $LP_{0,9}$ attenuation band reaches cut-off with increasing RI_{lyr}. This may be the condition when the ambient refractive index, a combined effective index of RI_{lyr} and n_{water}, becomes equal to the fiber clad index and before cut-off, the $\lambda_{0,9}$ increases for all T_{lyr}s with the increasing RI_{lyr}. This situation indicates that the LPG wavelength shift increases for all values of T_{lyr}, as the ambient index approaches the clad index. For the ambient index greater than the clad index, the higher-order LPG mode shows a considerably lesser sensitivity from the point of wavelength shift, but an effect on the attenuation band appearance can be observed [28, 50]. In this case, it was important to optimize both the

sensing layer parameters (T_{lyr} and RI_{lyr}) in such a way that the ambient index becomes close, indeed approaching the clad index.

The simulation outcome demonstrates that for a thick coating, T_{lyr} = 800 nm, the $LP_{0,9}$ attenuation band shows a 70 nm wavelength shift over a short RI_{lyr} range of 1.31 – 1.42, whereas, a comparatively smaller shift, $\Delta\lambda_{0,9}$ = 46.6 nm, was observed for a thin coating, T_{lyr} = 100 nm, but covering a wide RI_{lyr} range (1.31 – 1.72). The $LP_{0,9}$ attenuation band shows that a higher sensitivity is seen for the thicker sensing layer: however, the thicker the sensing layer, the narrower will be the RI_{lyr} range, illustrating the importance of this simulation in the optimization of physical and optical parameters of the sensing layer.

2.6 Sensing layer thickness optimization

Building on the results of the simulation, the $(CCS\text{-}NGO/PAA)_n$ multilayer coating was deposited through the scheme of LbL self-assembly (as discussed above and seen in Figs. 3(b, 1 – 3)). Following the depositions of the sensing layers, the LPG sections were examined using a Jeol JSM-6480LV Variable Pressure Analytical Scanning Electron Microscope (SEM) to determine the exact coating thickness and its surface morphology. A clear cross-sectional image of the coated-LPG is shown in Fig. 5(a). Figure 5(b) shows a magnified (×18,000) section of the $(CCS\text{-}NGO/PAA)_2$ multilayer coating film. T_{lyr} values were measured at fifteen different points of each image and finally, the mean, standard deviation (SD), and ±95% confidence interval in the (CI) values were calculated. Figure 5(c) shows the variation of the values of T_{lyr} with the deposited (CCS-NGO/PAA) layers, where the blue solid and red dashed lines represent the mean and ±95% CI values, respectively of T_{lyr}. The plot indicates that the T_{lyr} the value increases rapidly at the beginning and tends to saturate with the increasing numbers of complete CCS-NGO/PAA layers. Building on the simulation results (see Fig. 4), a 190.48 nm $(CCS\text{-}NGO/PAA)_1$-layer will have a lower sensitivity over a broad RI_{lyr} range, whereas a 571.60 nm $(CCS\text{-}NGO/PAA)_3$-layer will have a higher sensitivity, but for a short range of RI_{lyr}. Therefore, the thickness obtained after two complete cycles of deposition, i.e., $(CCS\text{-}NGO/PAA)_2$ was considered ideal for the sensing layer thickness (as shown in Fig. 5(b)) used in this study.

Thus, the optimized thickness of the sensing layer used was T_{lyr} = 390.56 nm (mean) $\pm$ 3.45 nm (SD) with a 95% CI = $\pm$6.76 nm, shown in the inset of Fig. 5(c). This thickness covers a maximum of 62.67 nm $\pm$ 95% CI (59.66 nm, 65 nm) wavelength shift ($\Delta\lambda_{0,9}$) over a RI_{lyr} range of 1.31 – 1.50.

Finally, a finite element-based modal simulation of PS1250/1500 SMF was also carried out in the COMSOL [51] platform to investigate the evanescent field strength before and after deposition of (CCS-NGO/PAA)$_2$ sensing layer. The results (illustrated in Fig. S2) show that the deposition of the sensing layer with a higher refractive index pulls the mode field towards itself, thus resulting in an extended and stronger evanescent light tail. A power confinement analysis [52] shows that after sensing layer deposition the evanescent field strength increased by 29 times compared to a bare LPG. Therefore, a strong evanescent light tail will improve the device sensitivity due to the enhanced light-matter interaction at the sensing layer.

3. Sensor Performance and System Analysis

The primary sensing probe consists of a nanocomposite material-coated LPG co-located with an FBG, as shown schematically in Fig. 1(a). The interrogation of the combined grating structure was carried out using an OSA coupled to a MATLAB-based signal processing program that is used to detect the LPG and FBG peak wavelengths, based on a calculation of the center of mass of the spectra [53].

3.1 Evaluation of sensor performance – temperature calibration

In this sensor system, the transmission peak of the FBG was used as a wavelength reference point from which the relative wavelength shift of the LP$_{0,9}$ attenuation band was measured. In a conventional FBG, the core and clad modes are not allowed by the fiber geometry to undergo mode coupling, and thus an FBG is intrinsically immune to changes in the ambient refractive index. However, the FBG was simultaneously utilized for temperature measurement when immersed in water and calibrated in a temperature-controlled oven, using for convenience a thermocouple, with data plotted in Fig. 6(a), for different water temperatures (from 21.1^{o}C to 50^{o}C). Figure 6(b) shows the temperature calibration curve where the red solid line and green dashed lines indicate the linear

fitting (R^2 = 0.999) and 95% confidence boundaries of the experimental data (with the temperature calibration factor being 29.603 pm/^{o}C).

3.2 Evaluation of sensor performance – Pb^{2+} ions in water

The complete water sensing probe was then evaluated in the detection of Pb^{2+} ions in water. To do so, a set of Pb^{2+} solutions, of eleven different concentrations (0.5 nM, 1 nM, 2 nM, 3 nM, 4 nM, 5 nM, 10 nM, 50 nM, 100 nM, 500 nM, and 1000 nM), was prepared by dissolving appropriate levels of lead nitrate salt in deionized (DI) water. The refractive indices of the Pb^{2+} solutions used were measured by using an Abbe refractometer, at a wavelength of 589 nm at room temperature (22^{o}C). The refractive index of the Pb^{2+} solution did not change with the ion concentrations mentioned above – a constant refractive index of 1.3325 was observed for all the nanomolar Pb^{2+} ions concentrations used. The sensor is able to monitor the change in the optical properties while trapping Pb^{2+} ions into the sensing layer (this being known as surface sensing).

In order to evaluate the performance, the fiber grating sensor probe was placed on a Teflon-based fluidic channel and a small volume (0.6 mL) of the aqueous solutions was carefully poured into a channel (using a pipette) to cover the entire sensor (grating) length – both sides of the fiber grating were tightly held by fiber clamps (to eliminate any strain effect on the gratings). In the calibration, first, the grating sensor was immersed in DI water to obtain a reference spectrum and then using the Pb^{2+} aqueous solutions (of different concentrations), the sensor was immersed for 20 minutes, and its spectral response was monitored. Prior to the next calibration, the sensor probe and the fluidic channel were fully washed with DI water and Figure 6(c) shows an offset spectrum (of the LPG and FBG) of the sensor ((CCS-NGO/PAA)$_2$ coated LPG and FBG) response, to different Pb^{2+} ion concentrations. The blue dotted indicates the centroid peak position of the attenuation band of the LPG, where the bottom blue curve shows the sensor spectrum for DI water only (i.e., 'zero' Pb^{2+}). As the adsorption of Pb^{2+} ions increases on the nanocomposite sensing layer, the corresponding LPG peak shifts towards longer wavelengths as the Pb^{2+} ions chelate with the key functional groups such as -NH_2, -OH, -COOH, and -SH of the CCS-NGO where the metal ion binds with the nitrogen and oxygen atoms through electron pair sharing. Due to the stronger lone pair electron attraction, the nitrogen atoms have a greater potential for donating the lone pair electron to heavy metal ions, to form a complex in comparison to oxygen atoms.

3.3 Pb^{+2} ions reactions with nanocomposite

The Pb^{2+} ions may react with the major -NH_2 functional group in the following ways:

$$R - NH_2 + Pb^{2+} \rightarrow R - NH_2Pb^{2+} \quad (2)$$

$$R - NH_3 + Pb^{2+} \rightarrow R - NH_2Pb^{2+} + H^+ \quad (3)$$

where R represents other chemical elements apart from the -NH_2 functional group. Equation 2 shows the formation of $R - NH_2Pb^{2+}$ complex due to the lone pair electron sharing of nitrogen atoms of the amino groups with the divalent Pb^{2+} ions. Additionally, the protonation of the amino group may occur and form $R - NH_3$ due to the water uptake in the (CCS-NGO/PAA)$_2$ sensing layer. However, Pb^{2+} ions may also attach to the nitrogen atoms of $R - NH_3$ through ion exchange [54, 55] as shown in Eq. 3. Further, being a borderline acidic element, Pb^{2+} ions are susceptible to be adsorbed selectively by the carboxyl and thiol groups [56] that appeared from CCS, PAA, and NGO, respectively. The complex reactions may increase or decrease the carboxyl and thiol groups in the composite, but the Pb^{2+} ion adsorption capacity remains unaffected due to the strong presence of the nitrogen atoms in CCS and NGO. While the sensor was immersed in water, the water uptake and Pb^{2+} ion adsorption increases the swelling degree of the (CCS-NGO/PAA)$_2$ nanocomposite. This decreases the refractive index of the (CCS-NGO/PAA)$_2$ sensing layer and corresponding spectral right-shift of the LPG sensor towards a longer wavelength.

As the Pb^{2+} ion concentration varied from 0 nM to 1000 nM, the LPG attenuation band showed a 22.23 nm spectral shift, highlighted in Fig. 6(c), indicating the Bragg wavelength (λ_{FBG}) (the reference peak from which the LPG spectral shifts were evaluated, and which is immune to changes in the metal ion concentrations). Figure 6(d) shows the relative spectral shift of LPG peaks from the FBG reference wavelength, for all twelve Pb^{2+} ion concentrations, showing the LPG peaks moving towards the reference line and showing this approach which has created a convenient and accurate evaluation of the wavelength shift.

3.4 Adsorption characteristics and binding affinity of metal ions to the adsorbent sensing layer

Following the experimental measurements carried out, adsorption isotherm models were used to explore the heterogeneous adsorption characteristics and binding affinity of metal ions to the

adsorbent sensing layer. Among the wide variety of equilibrium isotherm models [57, 58] available, six models such as Langmuir, Freundlich, Holl-Krich, Sips, Toth, and Khan were considered to explore the binding affinity of both low and high concentrations of selective Pb^{2+} ions. Figures 7(a) – (f) show the experimental data (blue circles) of $\Delta\lambda_{0,9}$ variation with Pb^{2+} concentrations (C) and their fittings (solid lines) by using Langmuir (LA), Freundlich (FR), Holl-Krich (HK), Sips (SI), Toth (TO), and Khan (KH) adsorption isotherm models on a logarithmic scale, respectively. The adsorption isotherm fitting plots over the complete concentration range in linear scale can be seen in Fig. S3. The fitted curves shown in Figs. 7(a) – (f) indicate that except for the Freundlich, all other isotherm models fitted well with the experimental data. The Holl-Krich, Sips, and Toth models yielded a very good fitting, with $R^2 > 0.98$, Langmuir and Khan with $R^2 > 0.97$, with the Freundlich model showing the worst fitting (with $R^2 = 0.8149$).

3.5 ANN-based sensor calibration

In order to create an accurate calibration, a forward nonlinear regression-based ANN model [36 – 38] was developed with two hidden layers of 20 nodes ($N_1^1 \dots N_{20}^1$ and $N_1^2 \dots N_{20}^2$) each to map the input parameters (I_1 and I_2) such as Pb^{2+} ion concentrations (C), and isotherm model and experimental data to the single-layer output (O_1) i.e., $LP_{0,9}$ attenuation band wavelength shift ($\Delta\lambda_{0,9}$). A set of figures in Figs. 8(a) – (e) depicts the ANN model framework and its outcomes for the evaluation of $\Delta\lambda_{0,9}$. The regression outcome in Fig. 8(b) showed that the predicted $\Delta\lambda_{0,9}$ values (shown by a 45° black line) are correlating well with the targeted actual $\Delta\lambda_{0,9}$ values (magenta circles). The ANN fitted curve correlated the predictions with the targeted vales as, $Predicted\ \Delta\lambda_{0,9} = 1 \cdot target\ \Delta\lambda_{0,9} - 2.8 \times 10^{-5}$ with a correlation coefficient value of R = 0.9999. Upon successful training, the regression-based ANN was then used as a calibration tool for accurate detection of $LP_{0,9}$ wavelength shift ($\Delta\lambda_{0,9}$) depending on the Pb^{2+} concentration. It can be observed that the ANN fitted calibration curve closely matched with the Toth isotherm model fitted values over the complete concentration range of 0 – 1000 nM, as shown in Fig. 8(c). The $(CCS\text{-}NGO/PAA)_2$ coated sensor was specially optimized for the detection of a lower concentration of heavy metal ions. Figure 8(d) shows the variation of $\Delta\lambda_{0,9}$ against the lower concentrations of Pb^{2+} ions (0 – 5 nM). As expected, the linear fitted calibration curve (blue line, $R^2 = 0.9969$) and ANN model (magenta line) showed a very good agreement with the experimental

data even in the lower concentration region. The slope of the linear fitted curve defines the sensitivity (S) of the device as S = 2.547±0.0637 nm/nM for the low concentration ion detection. The same ANN model was concurrently used to generate the calibration curve for the relative spectral shift i.e., $\Delta\lambda_R = |\lambda_{FBG} - \lambda_{0,9}^{LPG}|$, as shown in Fig. 8(e). It can be observed that the ANN fitted curve correlated (R = 0.9997) well with the Toth isotherm model which yields heterogeneous adsorption system for high as well as low adsorbate concentrations. From the theoretical perspective, the empirical equation of limit of detection (C_{LoD}) can be obtained by rearranging the Toth isotherm model by replacing the parameter C with C_{LoD}.

$$C_{LoD} = \frac{\Delta\lambda}{\left[K_{TO}^{n_{TO}} \cdot \left(\Delta\lambda_{max}^{n_{TO}} - \Delta\lambda^{n_{TO}}\right)\right]^{\frac{1}{n_{TO}}}} \tag{4}$$

where K_{TO}, n_{TO}, and $\Delta\lambda_{max}$ represent the Toth equilibrium isotherm constant under steady-state conditions, the isotherm model exponent, and the maximum wavelength shift while all the (CCS-NGO/PAA)2 binding sites are filled with metal ions, respectively. All these parametric values except $\Delta\lambda$ can be obtained from the fitting parameters of the Toth isotherm model. Throughout the experiment, the OSA spectral resolution was kept fixed as 0.5 nm. By considering all these parametric values and $\Delta\lambda$ = 0.5 nm, the C_{LoD} of the fiber grating-based Pb2+ ion sensor was calculated from Eq. 4 as 0.1783 nM (±95%: 0.1290 and 0.3459 nM). However, the smallest concentration measured by the sensor was 0.5 nM. Despite the theoretically obtained LoD from the Toth isotherm (showing a smaller value), the actual LoD can be stated to be 0.5 nM. It is worth mentioning that the C_{LoD} of the sensor proposed can be further improved by using the highest resolution i.e., $\Delta\lambda$ = 0.02 nm of the Yokogawa AQ6370C OSA used in this work. This indicates that the sensor can precisely trace a very small Pb^{2+} ion concentration which is well below the WHO recommended permissible limit i.e., 0.01 mg/L (48.31 nM), for drinking water [5]. Table 1 compares the key information such as sensing mechanisms, functionalized chemicals, and performance of the previously reported fiber-optic Pb^{2+} ion sensors with this work. In comparison with other published works, this CCS-NGO/PAA coated fiber grating sensor showed a promising result in the ultrasensitive detection of Pb^{2+} ions in potable water.

Table 1: Performance comparison of fiber optic Pb^{2+} ion sensors

LPG: Long period grating, TFBG: Tilted fiber Bragg grating, MMF: Multi-mode fiber, AuNP: Gold nanoparticles, PMO: Periodic mesoporous organosilica, BTESPTS: Bis [3-(triethoxysilyl) propyl] tetrasulfide, BP: Black Phosphorus, ITO: Indium tin-oxide, LSPR: Localized Surface Plasmon Resonance, SPR: Surface Plasmon Resonance, CS: Chitosan

Fiber sensing mechanism	**Sensing layer**	**Sensitivity**	**LoD**	**Operating range**	**Ref**
LPG	PMO/BTESPTS	2.072 nm/μM	-	0.086 μM	[59]
TFBG	BP	0.104 dB/μM	1.2 nM	0.5 nM – 7.24×10^{4} μM	[24]
Multimode fiber LSPR	AuNP/Monoclonal antibody	-	55.94 μM	0.048 – 0.48 μM	[60]
Multimode fiber LSPR	AuNP/1,1-Mercaptoundecanoic acid	0.28 nm/mM	800 μM	800 μM – 100 mM	[61]
Multimode fiber SPR	Pyrrole/CS/ITO/Ag	2.101 nm/nM	0.158 nM	0 – 200 μg/l	[62]
Multimode fiber SPR	Cu-film/Pb^{2+} imprinted NP	1.697×10^{4} nm/nM	0.2×10^{-4} nM	0 – 5 μM	[63]
Fiber-fluorescence sensor	DNAzyme	-	1.03 nM	2 – 75 nM	[64]
Hybrid fiber grating (LPG+FBG)	**CCS-NGO/PAA nanocomposite**	**2.547 nm/nM**	**0.5 nM**	**0.5 nM – 1000 μM**	**This work**

3.6 Investigation of Post-sensing surface morphology

The proficiency of $(CCS\text{-}NGO/PAA)_2$-coated LPG sensor in sensing Pb^{2+} ion was thoroughly investigated by examining the sensor coating surface morphology using the scanning electron microscope (SEM) and energy dispersive spectrometer (EDS). The spectrometry results were accumulated following the immersion of the coated fiber sensor to Pb^{2+} contaminated (10 nM) water and rinsed with DI water to remove the loosely bounded excess metal ions. Figures 9(a) – (e) show the SEM and EDS characterized data of the sensor. The EDS spectroscopic analyses were carried out on three rectangular areas (highlighted by magenta boxes) containing white random

smudges and two white points (marked by black arrows) indicated by S-1, S-2, S-3, and S-4, S-5, respectively as shown in Fig. 9(a) and inset Fig. 9(b). However, only the spectrum for S-2 is shown in Fig. 9(c) as evidence. The prominent peaks at 2.342 keV and 10.550 keV and multiple tiny peaks indicate the adsorption of Pb^{2+} ions onto the sensing layer. The spider plot in Fig. 9(d) shows the weight% analysis of different elements such as carbon (C), nitrogen (N), oxygen (O), silicon (Si), and especially, lead (Pb^{2+}) on different sites. A comparative high weight% of Pb^{2+} ions and lower weight% of other elements can be seen at points S-4 and S-5 as these points deliberately targeted the white dots which apparently indicated aggregations of Pb^{2+} ions. An almost similar weight% of Pb^{2+} can be seen for the three rectangular areas (S-1, S-2, and S-3). Thus undoubtedly, the newly appeared white patches implied a strong presence of Pb^{2+} ions. A normalized mean weight% with a standard error of mean (SEM) of the traced elements for all five sites were presented in Fig. 9(e). This represents an average distribution of different elements on the fiber sensor.

3.7 Dynamic response and specificity

Besides its sensing properties, the response time and reusability of the device are two salient features that indicate the ability of the sensor to detect the adsorption and desorption of targeted ions or molecules over a certain number of cycles. The response time depends on the chemical reactions i.e., the chelation and de-chelation rates of Pb^{2+} ions. The green curve in Fig. 10(a) shows the dynamic response of the sensor over three complete regeneration cycles. The fiber grating sensor was immersed in 5 nM Pb^{2+} ion contaminated water for 20 minutes until the spectral shift became stabilized with time, as shown by red circles. The fiber senor was then immersed in 1 mM EDTA solution for 20 minutes allowing the desorption of the metal ions. The black circles showed a higher spectral shift with abrupt fluctuations that may happen due to the change in the refractive index of the EDTA solution and the simultaneous desorption process of metal ions. Following that, the sensor was immersed in DI water, allowing a thorough wash. This section showed a rapid shift of the sensor response towards its initial position as the metal ions were desorbed and washed away from the sensing layer, as shown by the blue circles. Figures 10(b) and (c) show the experimental data and its fitted plots for the metal ion adsorption and desorption process, respectively, illustrating the effective adsorption time (t_{ads}) to be $t_{ads} = |t_{90} \sim t_{10}|_{rise} = 5.90$ min. On the other hand, the effective desorption time (t_{des}) was found to be $t_{des} = t_{EDTA}$ (20 min)

$+ |t_{90} \sim t_{10}|_{fall}$ (2.06 min) = 22.06 min. It is worth mentioning that during repetitive uses the sensor demonstrated a stable response. The standard deviation of the adsorption and desorption over three successive cycles was 0.0609 nm and 0.48817 nm, respectively. A slightly higher standard deviation during desorption indicated the accumulation of a very small amount of Pb^{2+} ions that were permanently trapped due to repetitive uses. Moreover, faster desorption can be achieved using a stronger EDTA solution, but it may compromise the sensor lifetime.

Different chelating agents of the sensing layer have the potentials to react with and adsorb different heavy metal ions depending on their binding affinities [65, 66]. To investigate that, fiber sensor was tested with different solutions of heavy metal ions (Pb^{2+}, Hg^{2+}, Cu^{2+}, Cd^{2+}, Cr^{3+}, Na^{+} - of the same 5 nM concentrations). The $LP_{0,9}$ attenuation band shift ($\Delta\lambda_{0,9}$) under different metal ion environments have been compared and plotted in Fig. 10 (d). A comparatively high value of $\Delta\lambda_{0,9}$ was observed only for the Pb^{2+} ion and a moderate but yet low response can be seen for the Hg^{2+} ion. A much lower response can be seen for Cu^{2+}, Cd^{2+}, Cr^{3+}, and almost a negligible wavelength shift was seen for Na^{+} ions. Thus, the experimental data reveals that the richness of multiple chelating binding sites in NGO-functionalized cross-linked chitosan nanocomposite made it susceptible to specifically adsorb the Pb^{2+} ions compared to other metal ions, showing its capability for selective sensing and extraction of Pb^{2+} ions from the compound solution.

3.8 Spike and recovery study

To investigate the sensor performance with an actual 'tap water' sample, a spike and recovery study was carried out. Pb^{2+} ion contaminated water samples of three different concentrations were tested and being recovered by the developed sensor. The spiked Pb^{2+}test samples and their recovery results are tabulated in Table 2. The experiment shows that the developed sensor can detect and recover 95.05% - 98.72% of Pb^{2+} ions from the test samples with the relative error of 2.48% - 12.86%, respectively. Corresponding sensitivity variation obtained agreed with the predetermined sensitivity value. The results summarized below indicate the reliability of the sensor attributes examined under practical conditions.

Table 2: Spike and recovery studies in the real tap water samples.

Externally added Pb^{2+} (nM)	Detected Pb^{2+} (nM)	Recovery (%)	Relative Error (%)	Sensitivity (nm/nM)
0.5	0.475 ± 0.0089	95.05	2.48	2.588
5	4.866 ± 0.0414	97.32	13.43	2.624
10	9.872 ± 0.1963	98.72	12.85	1.786

4. Conclusion

In this work, a nanocomposite functionalized robust and flexible fiber optic hybrid multi-grating sensor, operating on the $LP_{0,9}$ attenuation band of an LPG and with a temperature and wavelength reference FBG (written at λ_B = 1524 nm), has been designed, developed and evaluated, incorporating an ANN, to create an effective, sensitive lead (Pb^{2+}) ion sensor. The sensor working principle was based on a strong light-matter interaction between the evanescent field of a higher-order clad mode and the surrounding refractometric variation, arising due to selective adsorption of the heavy metal ion. The sensor was created through a layer-by-layer assembly of CCS-NGO/PAA multilayer overlay, giving the device the required selectivity to Pb^{2+} ions. The sensor system was optimized by tailoring the sensing layer thickness to achieve an effective sensitivity as high as 2.55 ± 0.06365 nm/nM (with a detection limit of 0.5 nM). To improve the sensor performance, an ANN-based calibration tool has been developed and implemented for the accurate prediction of the nonlinear responses of the sensor that may arise due to the heterogenous metal ion adsorption.

In ongoing work, the aim is now to explore the nano-layer deposition of alternative materials that can be optimized to immobilize and therefore sense other heavy metals and toxic substances, commonly found in an aquatic environment. Furthermore, it is considered that the device sensitivity could be improved by using a dual-resonance peak LPG in order to exploit the response of the higher-order clad modes. Further, an environment-friendly smart sensor packaging designed to prevent biofouling and the introduction of artificial intelligence assisted cloud-based remote interrogation technique is proposed to create a sensor system designed as a portable high-throughput fiber-based water quality monitoring device for in-the-field use.

Declaration of competing interest

The authors declare that there are no conflicts of interest.

Acknowledgements

This work was funded and supported by the Natural Environment Research Council (NERC) (NE/R003289) and City, University of London, UK. The authors thank Jim Davy and Dr. Andrew R. Thomson from the University College London for insightful discussion and support for the Scanning Electron Microscope imaging and FT-IR spectroscopy, respectively. K. T. V. Grattan and T. Sun acknowledge support from the Royal Academy of Engineering, UK.

References

[1] United Nations Sustainable Development, About the sustainable development goals

[2] WHO, Guidelines for Drinking Water Quality, World Health Organization, 2011, Retrieved from http://www.who.int/water_sanitation_health/dwq/gdwq0506.pdf

[3] C. V. Mosby, W. D. Glanze, K. N. Anderson, Mosby Medical Encyclopedia, The Signet: Revised Edition, St. Louis

[4] M. Jaishankar, T. Tseten, N. Anbalagan, B. B. Mathew, and K. N. Beeregowda, Toxicity mechanism and health effects of some heavy metals, Interdiscip. Toxicol., 7 (2014) 60 – 72

[5] S. J. S. Flora and V. Pachauri, Chelation in metal intoxication, Int. J. Environ. Res. Health, 7 (2010) 2745 – 2788

[6] Y. Zhang, Y. Sun, L. Cai, Y. Gao, and Y. Cai, Optical fiber sensors for measurement of heavy metal ion concentration: A review, Measurement, 158 (2020) 107742

[7] M. Yin, B. Gu, Q-F. An, C. Yang, Y. L. Guan, and K-T. Yong, Recent development of fiber-optic chemical sensors and biosensors: Mechanisms, materials, micro/nano-fabrications and applications, Coord. Chem. Rev., 376 (2018) 348 – 392

[8] B. Rente, M. Fabian, Y. Chen. L. Vorreiter, H. Bustamante, T. Sun, K. T. V. Grattan, In-sewer field-evaluation of an optical fiber-based condition monitoring system, IEEE Sens. J. 20 (2020) 2976 – 2981

[9] V. N. K. Pabbisetti, S. S. Madhuvarasu, Hydrogel-coated fiber Bragg grating sensor for pH monitoring, Opt. Eng. 55 (2016) 066112

[10] Kavita B S, Sridevi S, P Makam, D Ghosh, T Govindaraju, S Asokan, A K Sood, Highly sensitive and rapid detection of mercury in water using functionalized etched fiber Bragg grating sensors, Sens. Actuat., B: Chem. 333 (2021) 129550

[11] C. Bian, M. Hu, R. Wang, T. Gang, R. Tong, L. Zhang, T. Guo, X. Liu, X. Qiao, Optical fiber humidity sensor based on the direct response of the polyimide film, Appl. Opt. 57 (2018) 356 – 361

[12] Q. Sun, X. Sun, W. Jia, Z. Xu, H. Luo, D. Liu, L. Zhang, Graphene-assisted microfiber for optical-power based temperature sensor, IEEE Photonics Technol. Lett. 28 (2016) 383–386.

[13] S. Chandra, Dhawangale Arvind, S. Mukherji, Hand-held optical sensor using denatured antibody coated electro-active polymer for ultra-trace detection of copper in blood serum and environmental samples, Biosens. Bioelectron. 110 (2018) 38 – 43

[14] M-Y. Ye, M-X. Shen, X-M. Lin, Ringing phenomenon based whispering-gallery-mode sensing, Sci. Rep. 6 (2016) 19597

[15] Z. Zhu, L. Liu, Z. Liu, Y. Zhang, Y. Zhang, Surface-plasmon-resonance based optical-fiber temperature sensor with high sensitivity and high figure of merit, Opt. Lett. 42 (2017) 2948 – 2951.

[16] S. Weng, L. Pei, J. Wang, T. Ning, J. Li, High sensitivity D-shaped hole fiber temperature sensor based on surface plasmon resonance with liquid filling, Photon. Res. 5 (2017) 2948 – 2951.

[17] E. B-Pena, M. G. Valdes, B. G-Martinez, M. C. M-Bondi, Fluorescence based fiber optic and planar waveguide biosensors: A review, Anal. Chim. Acta. 943 (2016) 17 – 40.

[18] M. Deng, L. Liu, Y. Zhao, G. Yin, T. Zhu, Highly sensitive temperature sensor based on an ultra-compact Mach-Zehnder interferometer with side-opened channels, Opt. Lett. 42 (2017) 3549 – 3552.

[19] B. Gu, M. Yin, A. P. Zhang, J-W. Qian, S. He, Fiber-optic metal ion sensor based on thin-core fiber modal interferometer with nanocoating self-assembled via hydrogen bonding, Sens. Actuators B: Chem. 160 (2011) 1174 – 1179

[20] W. B. Ji, S. H. K. Yap, N. Panwar, L. L. Zhang, B. Lin, K. T. Yong, S. C. Tjin, W. J. Ng, M. B. A. Majid, Detection of low-concentration heavy metal ions using optical microfiber sensor, Sens. Actuat., B: Chem. 237 (2016) 142 – 149.

[21] N. Zhong, Z. Wang, M. Chen, X. Xin, R. Wu, Y. Cen, Y. Li, Three-layer-structure polymer optical fiber with a rough inter-layer surface as a highly sensitive evanescent wave sensor, Sens. Actuators B Chem. 254 (2018) 133 – 142

[22] T. H. Nguyen, T. Sun, K. T. V. Grattan, A turn-on fluorescence-based fiber optic sensor for the detection mercury, Sensors 19 (2019) 2142

[23] Y. Si, J. Lao, X. Zhang, Y. Liu, S. Cai, A. González-Vila, K. Li, Y. Huang, Y. Yuan, C. Caucheteur, and T. Guo, Electrochemical plasmonic fiber-optic sensors for ultra-sensitive heavy metal detection, J. Lightwave Technol., 37(2019), 3495 – 3502

[24] C. Liu, Z. Sun, L. Zhang, J. Lv, X. F. Yu, L. Zhang, and X. Chen, Black phosphorous integrated tilted fiber grating for ultrasensitive heavy metal sensing, Sens. Actuators B: Chem. 257 (2018) 1093 – 1098

[25] R. Tabassum, B. D. Gupta, Fiber optic manganese ions sensor using SPR and nanocomposite of ZnO-polypyrrole, Sens. Actuators B: Chem. 220 (1) (2015) 903–909.

[26] A. K. Sharma, R. Jha, B. D. Gupta, Fiber-optic sensors based on surface plasmon resonance: a comprehensive review, IEEE Sens. J. 7 (8) (2007) 1118–1129.

[27] I. D. Villar, I. R. Matias, F. J. Arregui, and P. Lalanne, Optimization of sensitivity in long period gratings with overlay deposition, Opt. Express 13 (2005) 56 – 69

[28] H. J. Patrick, A. D. Kersey, and F. Bucholtz, Analysis of the response of long period fiber gratings to external index of refraction, J. Lightwave Technol. 16 (1998) 1606 – 1612

[29] N. D. Rees, S. W. James, R. P. Tatam, and G. J. Ashwell, Optical fiber long-period gratings with Langmuir-Blodgett thin-film overlays, Opt. Lett. 27 (2002) 686 – 688

[30] S. W. James and R. P. Tatam, Optical fiber long-period grating sensors: characteristics and application, Meas. Sci. Technol. 14 (2003) R49 – R61

[31] M. Jiang, A. P. Zhang, Y. C. Wang, H. Y. Tam, and S. He, 2009. Fabrication of a compact reflective long-period grating sensor with a cladding-mode-selective fiber end-face mirror, Opt. Express, 17 (2009) 17976 – 17982

[32] G. Quero, S. Zuppolini, M. Consales, L. Diodato, P. Vaiano, A. Venturelli, M. Santucci, F. Spyrakis, M. P. Costi, M. Giordano, A. Borriello, A. Cutolo, and A. Cusano, Long period fiber grating working in reflection mode as valuable biosensing platform for the detection of drug resistant bacteria." Sens. Actuators B: Chem. 230 (2016) 510 – 520

[33] S. Sridevi, K. S. Vasu, N. Jayaraman, S. Asokan, A. K. Sood, Optical bio-sensing devices based on etched fiber Bragg gratings coated with carbon nanotubes and graphene oxide along with a specific dendrimer, Sens. Actuators B: Chem. 195 (2014) 150 – 155.

[34] S. Korposh, S. W. James, S-W. Lee, R. P. Tatam, Tapered optical fiber sensors: current trends and future perspectives, Sensors 19 (2019) 2294

[35] Z-W. Ding, R. Ravikumar, C-L. Zhao, L-H. Chen, C-C. Chan, Chitosan/poly (acrylic acid) based fiber-optic surface plasmon resonance sensor for Cu^{2+} ions detection, J. Lightwave Technol. 37 (2019) 2246 – 2252

[36] S. Chugh, S. Ghosh, A. Gulistan, B. M. A. Rahman, Machine learning regression approach to the nanophotonic waveguide analyses, J. Lightwave Technol., 37 (2019) 6080 – 6089

[37] S. Chugh, A. Gulistan, S. Ghosh, B. M. A. Rahman, Machine learning approach for computing optical properties of a photonic crystal fiber, Opt. Express 27 (2019) 36414 – 36425

[38] R. S. Hegde, Deep learning: a new tool for photonic nanostructure design, Nanoscale Advances 2 (2020) 1007 – 1023

[39] R. Kashyap, Fiber Bragg Gratings, Academic press, 2009.

[40] R. Scott, M. Vidakovic, S. Chikermane, B. McKinley, T. Sun, P. Banerji, and K. T. V. Grattan, Encapsulation of fiber optic sensors in 3-D printed packages for use in civil engineering applications: a preliminary study, Sensors 19 (2019) 1689-1 – 13

[41] K. P. W. Dissanayake, W. Wu, H. Nguyen, T. Sun, and K. T. V. Grattan, Graphene-oxide-coated long-period grating-based fiber optic sensor for relative humidity and external refractive index, J. Lightwave Technol. 36 (2017) 1145 – 1151

[42] OptiGrating v4.2.3, Optiwave Systems Inc., "https://optiwave.com/optigrating-overview/"

[43] F. H. Baldovino, A. T. Quitain, N. P. Dugos, S. A. Roces, M. Koinuma, M. Yuasa, T. Kida, Synthesis and characterization of nitrogen-functionalized graphene oxide in high-temperature and high-pressure ammonia, RSC Advances, 6 (2016) 113924 – 113932

[44] P. Pilla, V. Malachovska, A. Borriello, A. Buosciolo, M. Giordano, L. Ambrosio, A. Cutolo, and A. Cusano, Transition mode long period grating biosensor with functional multilayer coatings, Opt. Express 19 (2011) 512 – 526

[45] L. Zhang, Y. Zeng, Z. Cheng, Removal of heavy metal ions using chitosan and modified chitosan: A review, J. Mol. Liq. 214 (2016) 175 – 191

[46] N. R. Kildeeva, P. A. Perminov, L. A. Vladimirov, V. V. Novikov, and S. N. Mikhailov, About mechanism of chitosan cross-linking with glutaraldehyde, Russ. J. Bioorg. Chem. 35 (2009) 360 – 369, DOI: 10.1134/S106816200903011X

[47] A. C. Oyrton, Monteiro Jr., C. Airoldi, Some studies of crosslinking chitosan – glutaraldehyde interaction in a homogeneous system, Int. J. Biol. Macromol. 26 (1999) 119 – 128, DOI: 10.1016/S0141-8130(99)00068-9

[48] T. B. Pham, H. Bui, H. T. Le, and V. H. Pham, Characteristics of the fiber laser sensor system based on etched-Bragg grating sensing probe for determination of the low nitrate concentration in water, Sensor 17 (2017) 1 – 9.

[49] S. Bandyopadhyay, I. D. Villar, N. Basumallick, P. Biswas, T. K. Dey, S. Bandopadhyay, Long period fiber grating for biosensing: an improved design methodology to enhance add-layer sensitivity, J. Lightwave Technol. 36 (2018) 1178 – 1184

[50] B. H. Lee, Y. Liu, S. B. Lee, S. S. Choi, Displacement of the resonant peaks of a long-period fiber grating induced by a change of ambient refractive index, Opt. Lett. 22 (1997) 1769 – 1771, DOI: 10.1364/ol.22.001769

[51] Wave Optics Module User's Guide, version 5.5, COMSOL, Inc, https://www.comsol.com

[52] S. Ghosh, B. M. A. Rahman, Design of on-chip hybrid plasmonic Mach-Zehnder interferometer for temperature and concentration detection of chemical solution, Sens. Actuat., B: Chem. 279 (2019) 490 – 502

[53] D. Tosi, Review and analysis of peak tracking techniques for fiber Bragg grating sensors, Sensors 17 (2017) 1 – 35, DOI: 10.3390/s17102368

[54] E. Onsoyen, O. Skaugrud, Metal recovery using chitosan, J. Chem. Technol. Biotechnol. 49 (1990) 395 – 404, DOI: 10.1002/jctb.280490410

[55] L. Jin, R. Bai, Mechanisms of lead adsorption on chitosan/PVA hydrogel beads, Langmuir 18 (2002) 9765 – 9770, DOI: 10.1021/la025917l

[56] J. Fan C. Cai, H. Chi, B. J. Reid, F. Coulon, Y. Zhang, and Y. Hou, Remediation of cadmium and lead polluted soil using thiol-modified biochar, J. Hazard. Mater. 388 (2019) 122037 – 1 – 11, DOI: 10.1016/j.jhazmat.2020.122037

[57] N. Ayawei, A. N. Ebelegi, D. Wankasi, Modelling and interpretation of adsorption isotherms, J. Chem. (2017) 1 – 11, DOI: 10.1155/2017/3039817

[58] K. Y. Foo and B. H. Hameed, Insights into the modeling of adsorption isotherm systems, Chem. Eng. J. 156 (2010) 2 – 10, DOI: 10.1016/j.cej.2009.09.013

[59] J. Du, J. Cipot-Wechsler, J. M. Lobez, H-P. Loock, and C. M. Crudden, Periodic mesoporous organosilica films: key components of fiber-optic-based heavy-metal sensors, Small 6(11) (2010) 1168 – 1172

[60] T-J. Lin and M-F. Chung, Using monoclonal antibody to determine lead ions with a localized surface plasmon resonance fiber-optic biosensor, Sensors 8 (2008) 582 – 593

[61] P. Dhara, R. Kumar, L. Binetti, H. T. Nguyen, L. S. Alwis, T. Sun, K. T. V. Grattan, Optical fiber-based heavy metal detection using the localized surface plasmon resonance technique, IEEE Sens. J. 19 (19) (2019) 8720 – 8726

[62] R. Verma, B. D. Gupta, Detection of heavy metal ions in contaminated water by surface plasmon resonance based optical fiber sensor using conducting polymer and chitosan, Food Chem. 166 (2015) 568 – 575

[63] A. M. Shrivastav, B. D. Gupta, Ion-imprinted nanoparticles for the concurrent estimation of Pb(II) and Cu(II) ions over a two channel surface plasmon resonance fiber-optic platform, J. Biomed. Opt. 23 (2018) 1 – 8

[64] N. Yildirim, F. Long, M. He, C. Gao, H-C. Shi, A portable DNAzyme-based optical biosensor for highly sensitive and selective detection of lead(II) in water sample, Talanta, 129(21) (2014) 617 – 622

[65] N. H. Kamaruddin, A. A. A. Bakar, N. N. Mobarak, M. S. D. Zan, and N. Arsad, Binding affinity of a highly sensitive Au/Ag/Au/chitosan-graphene oxide sensor based on direct detection of Pb^{2+} and Hg^{2+} ions, Sensors 17 (2017) 1 – 16, DOI: 10.3390/s17102277

[66] Z. Chen, K. Han, Y-N. Zhang, Reflective fiber surface plasmon resonance sensor for high-sensitive mercury ion detection, Appl. Sci. 9 (2019) 1480

Figures and captions

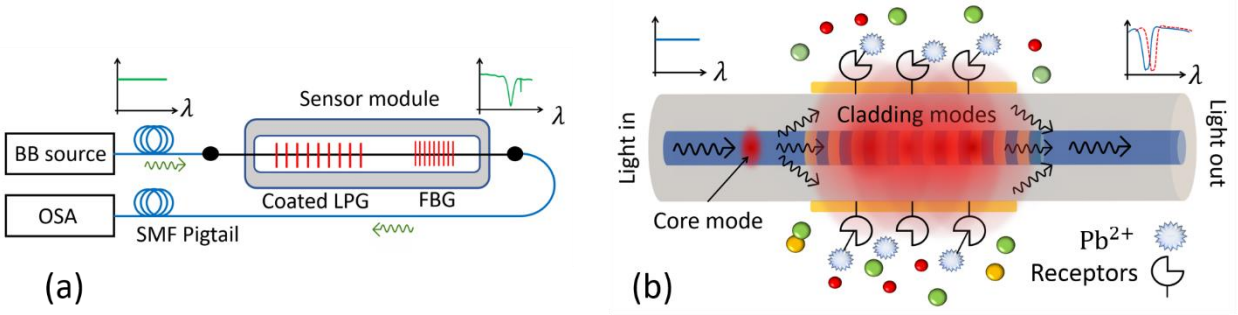

Figure 1: (a) Schematic diagram of fiber optic hybrid grating (butt-coupled LPG and FBG) sensor set-up for simultaneous detection of lead (Pb^{2+}) ion and water temperature. Inset shows the transmission spectra of the hybrid fiber optic grating. Big and peak is from LPG and the small peak is from FBG. (b) illustrates the working principle of an LPG. Periodic refractive index modulation in fiber core excites the lossy cladding modes. Mode couplings between core and fiber clad modes result in multiple attenuation bands at distinct wavelengths.

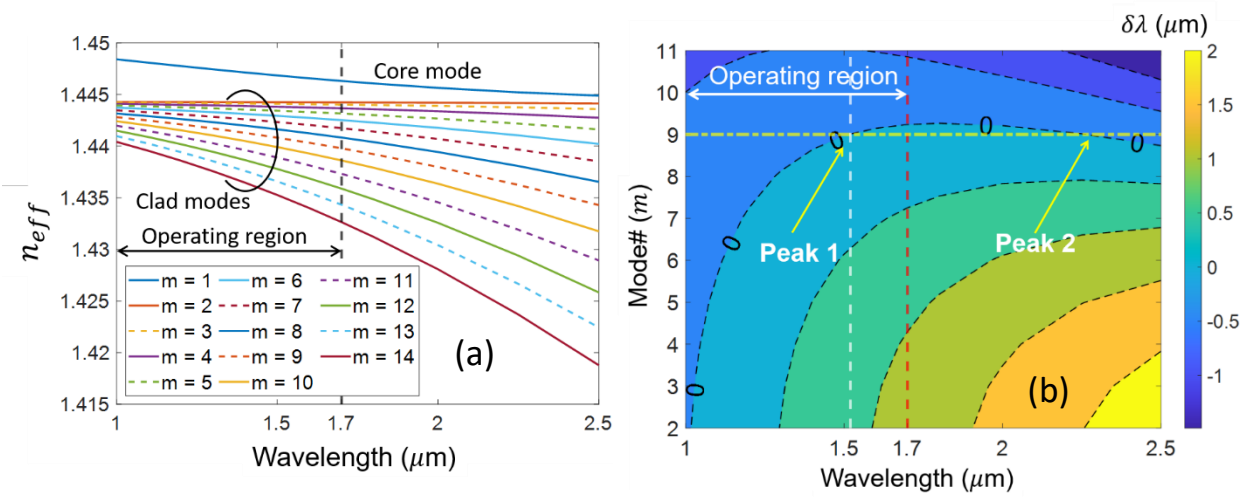

Figure 2: Simulation results. (a) Effective index (n_{eff}) dispersion of the core and clad modes (m = 1, 2, 3, …14) of the silica-clad single-mode optical fiber (PS1250/1500). The core mode (m = 1) showed a higher n_{eff} than the clad modes. (b) The surface plot illustrates the behavior of the wavelength difference ($\delta\lambda$) of each LPG resonant modes with the operating wavelength. $\delta\lambda$ = 0 is represented by the zero marked black dashed line. The double zero-crossing of the $LP_{0,9}$ mode (yellow dashed-dotted line) signified its dual-peak nature. Peak 1 is situated in the S-band region and Peak 2 is around 2.4 μm. Peak 1 was within the operating region of the source and detector, therefore used for sensing.

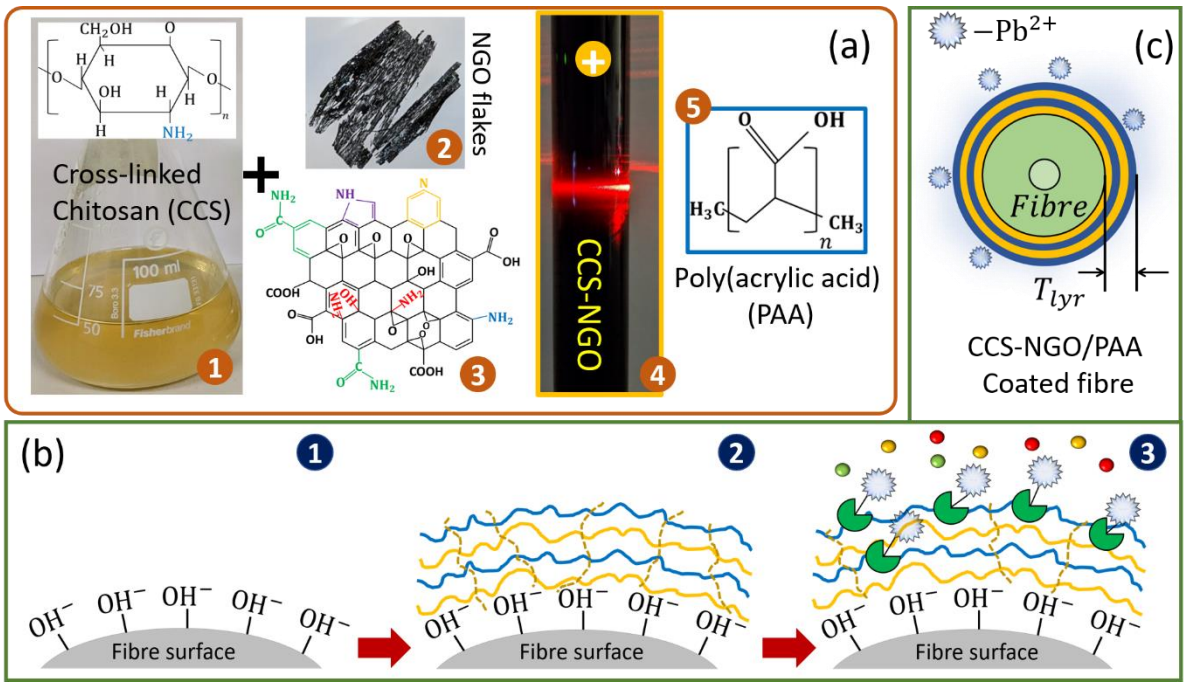

Fig. 3 (a) Photos of as-prepared chemicals used to develop the sensor, (1) shows freshly prepared glutaraldehyde cross-linked chitosan (CCS), (2) and (3) depict the flakes and chemical structure of nitrogen-doped graphene oxide (NGO), respectively, (4) shows a freshly prepared cationic CCS-NGO nanocomposite illuminated by He-Ne laser beam, demonstrating Tyndall effect (5) shows the chemical structure of anionic poly(acrylic acid) (PAA). (b) Schematic diagram of surface modification steps of LPG, starting from hydroxylation (1), layer-by-layer (LbL) self-assembly of CCS-NGO/PAA layers (2), and lead (Pb^{2+}) ion detection by the nanocomposite overlay (3); (c) impression of $(CCS\text{-}NGO/PAA)_2$-coated fiber sensor for the Pb^{2+} ion detection.

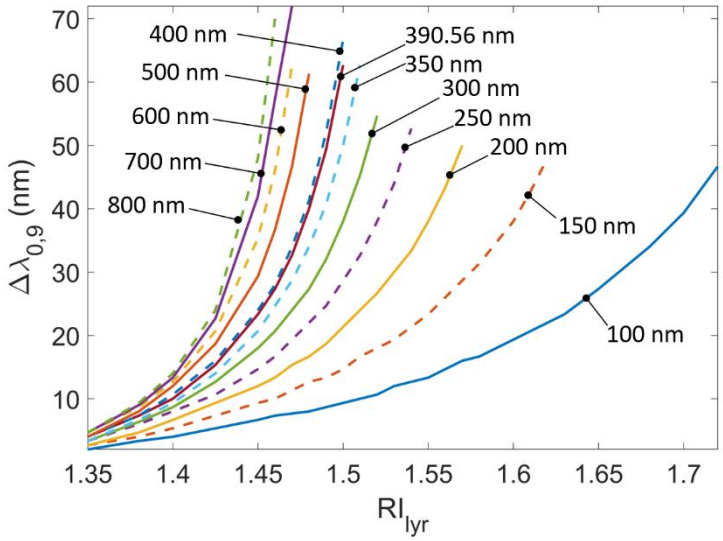

Figure 4: Simulation results shows the wavelength shift ($\Delta\lambda_{0,9}$) of $LP_{0,9}$ attenuation band depending on the variation of thickness (T_{lyr}) and refractive index (R_{lyr}) of the sensing layer. The considered ranges for the T_{lyr} and RI_{lyr} were 100 nm – 800 nm and 1.35 – 1.72, respectively. The $\Delta\lambda_{0,9}$ variation for the optimized T_{lyr} = 390.56 nm over a RI_{lyr} range of 1.35 – 1.50, is shown in the plot.

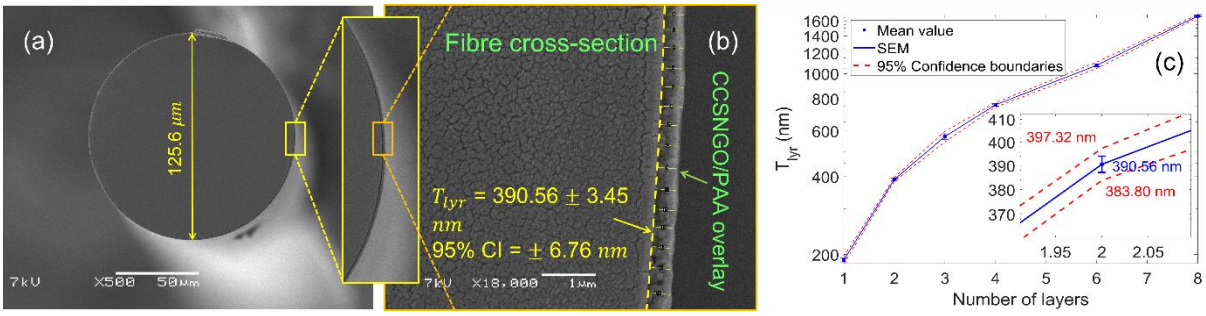

Figure 5. Scanning Electron Microscopic (SEM) image of the $(CCS\text{-}NGO/PAA)_2$ coated LPG. (a) A section of the coated LPG was attached to the sides of a nut placed on a SEM stub. This arrangement helped in fiber cross-sectional imaging (b) and coating thickness (T_{lyr}) measurement. (c) 18,000 times zoomed image shows a close view of the nanocomposite overlay, suitable for T_{lyr} measurement. (d) The plot depicts the variation of CCS-NGO/PAA overlay thickness with the number of deposited layers. T_{lyr} increased rapidly and showed a saturation trend after the 3rd layer. The inset shows the optimized $(CCS\text{-}NGO/PAA)_2$-layer thickness of 390.56 nm with 95% confidence boundaries that varied from 383.80 nm to 397.32 nm.

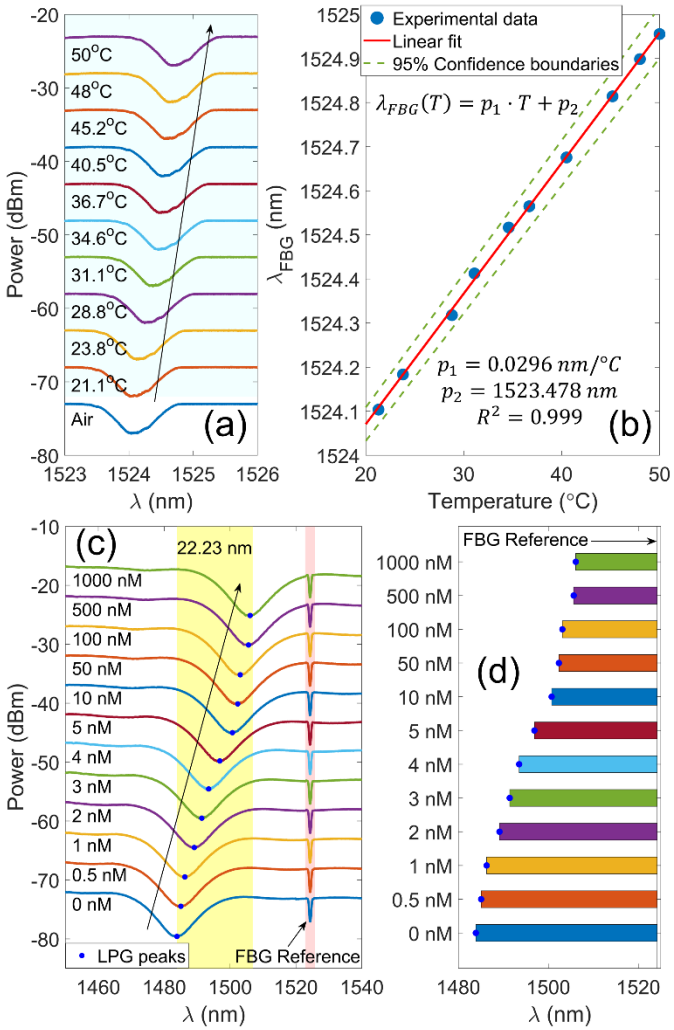

Figure 6: Spectral responses of the LPG and FBG. (a) Bragg wavelength shift (λ_{FBG}) depending on water temperature varied from 21.1ºC to 50ºC. The bottom blue spectrum shows the FBG response while it was in the air at room temperature. (b) depicts a linear shift of λ_{FBG} with the water temperature increment. The red solid and green dashed lines indicate the linear fitting with a fitness value of R^2 = 0.9992 and 95% confidence interval, respectively. (c) represents the complete sensor response. The wide and sharp peaks depict the attenuation band of the $(CCS\text{-}NGO/PAA)_2$ coated LPG and bare FBG, respectively. The coated LPG showed a spectral shift towards a higher wavelength with the variation of Pb^{2+} ion concentration (0 nM to 1000 nM) in water. The λ_{FBG} was used as a reference point from which a relative spectral shift ($\Delta\lambda_R$) of the LPG was measured. (d) represents a bar chart showing the relative spectral shift ($\Delta\lambda_R$) of LPG from the FBG reference point for different Pb^{2+} ion concentration in water.

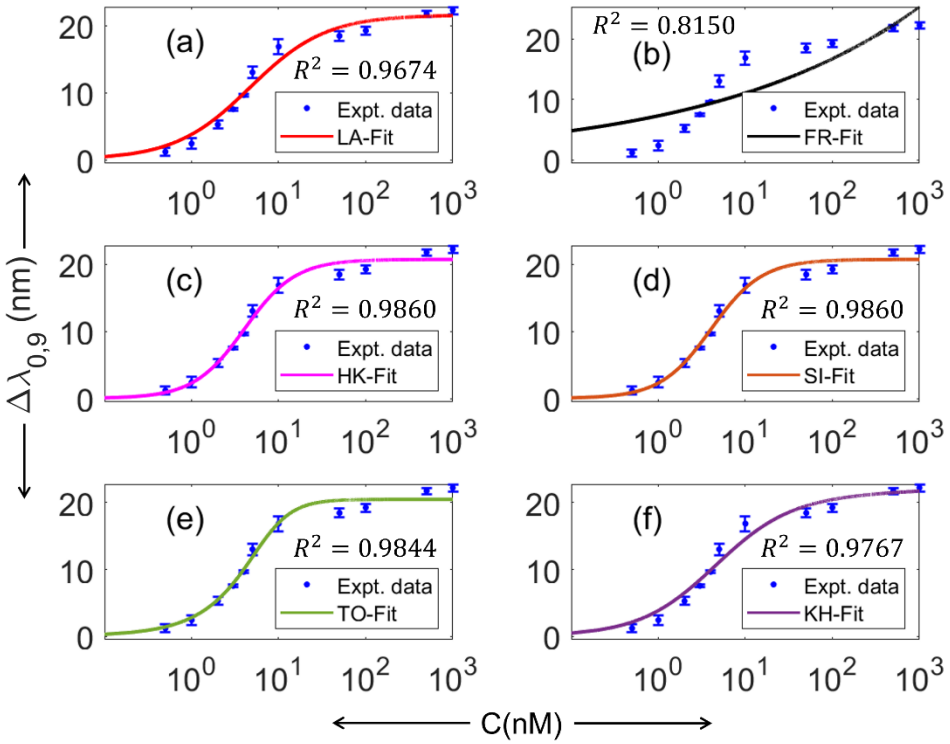

Figure 7: Adsorption isotherm fitting of the $LP_{0,9}$ peak shifts ($\Delta\lambda_{0,9}$) depending on the concentration (C in nM) of Pb^{2+} ion. Subplot (a) shows Langmuir (LA), (b) Freundlich (FR), (c) Holl-Krich (HK), (d) Sips (SI), (e) Toth (TO) isotherm fit, and (f) Khan (KH) isotherm fit. See Fig. S3 in the supplementary material for the isotherm fitting over a complete concentration range of 0 nM – 1000 nM in linear scale.

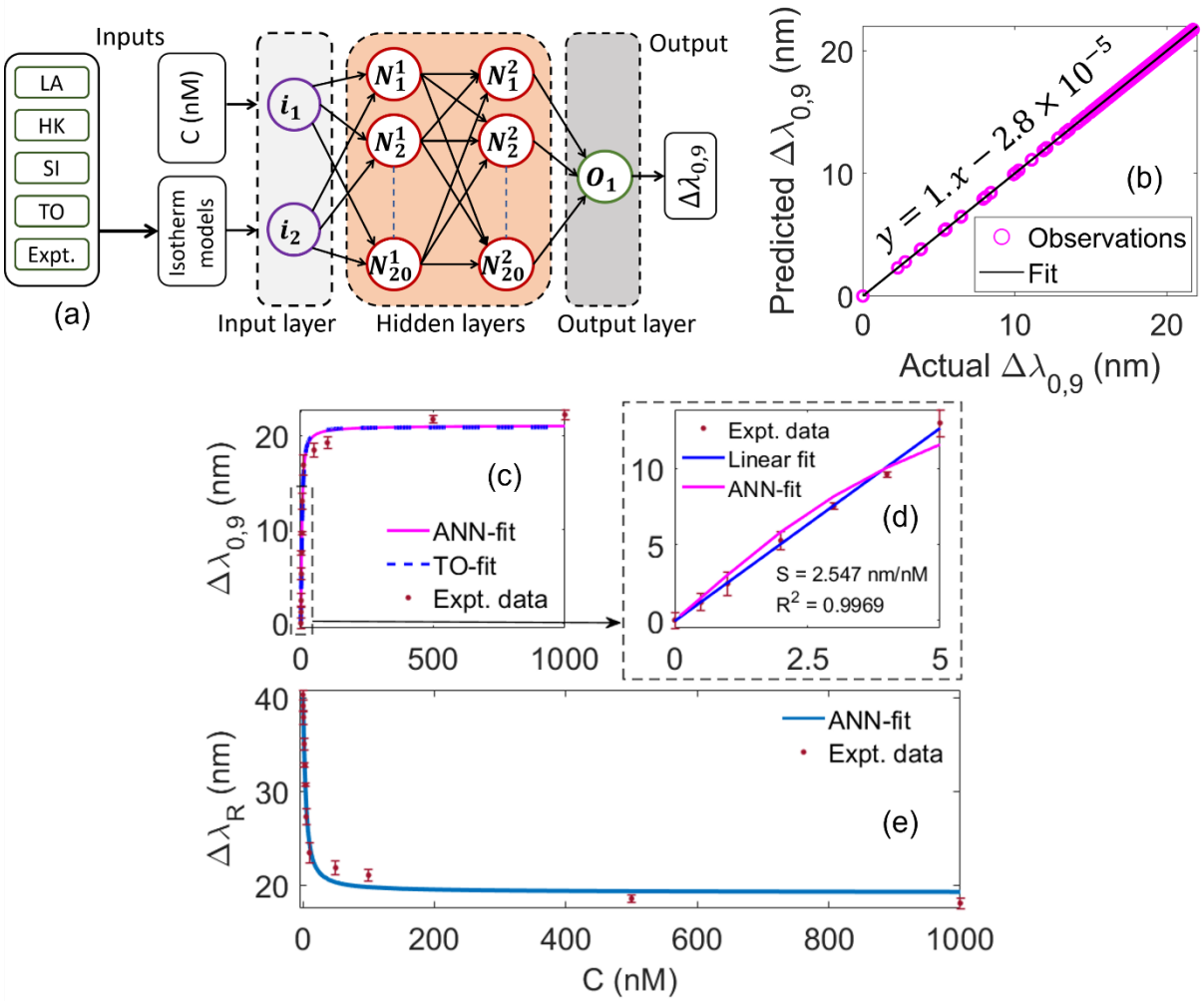

Figure 8: A forward ANN model to calibrate the nonlinear response of the Pb^{2+} ion sensor. (a) Block diagram of ANN architecture. (b) Regression plot shows a correlation between actual and predicted $\Delta\lambda_{0,9}$ with a coefficient value of R = 0.9999 and within the error limit of -1×10^{-4} to $+1\times10^{4}$. (c) Variation of LPG wavelength shift ($\Delta\lambda_{0,9}$) with Pb^{2+} ion concentration (C). (d) shows a linear response of the sensor for the detection very low concentration (0 – 5 nM) of Pb^{2+} ions. Both ANN predicted and Toth isotherm fitted curves demonstrated an excellent agreement with the experimental data. (e) Variation of relative wavelength shift ($\Delta\lambda_R = |\lambda_{FBG} - \lambda_{0,9}^{LPG}|$) with the Pb^{2+} ion concentration. The ANN predicted nonlinear response of the sensor was in good agreement with the actual experimental data.

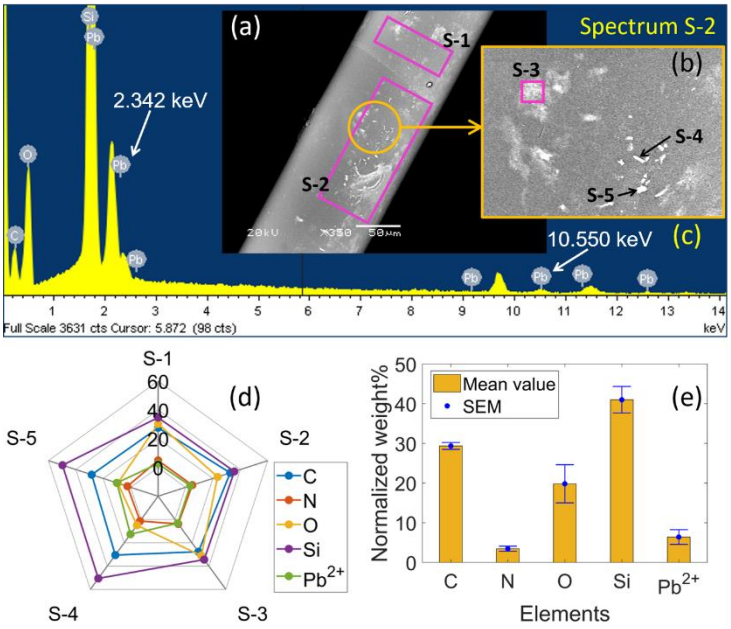

Figure 9: SEM and EDS analysis of the fiber sensor after Pb^{2+} sensing. (a) and inset (b) depict SEM images of the coated fiber surface. The white smudges represent the adsorption and aggregation of Pb^{2+} ions on the sensing layer. Five sites (S-1, S-2, S-3, S-4, and S-5) were selected for EDS analysis. Three rectangular areas and two points were marked by magenta lines and black arrows. (c) presents the spectrum of S-2, a broad area of sensing layer. (d) and (e) represent the spider and bar plots of site-wise and mean weight%, respectively, of traced elements such as carbon (C), nitrogen (N), oxygen (O), silicon (Si), and lead (Pb^{2+}) on the sensing layer.

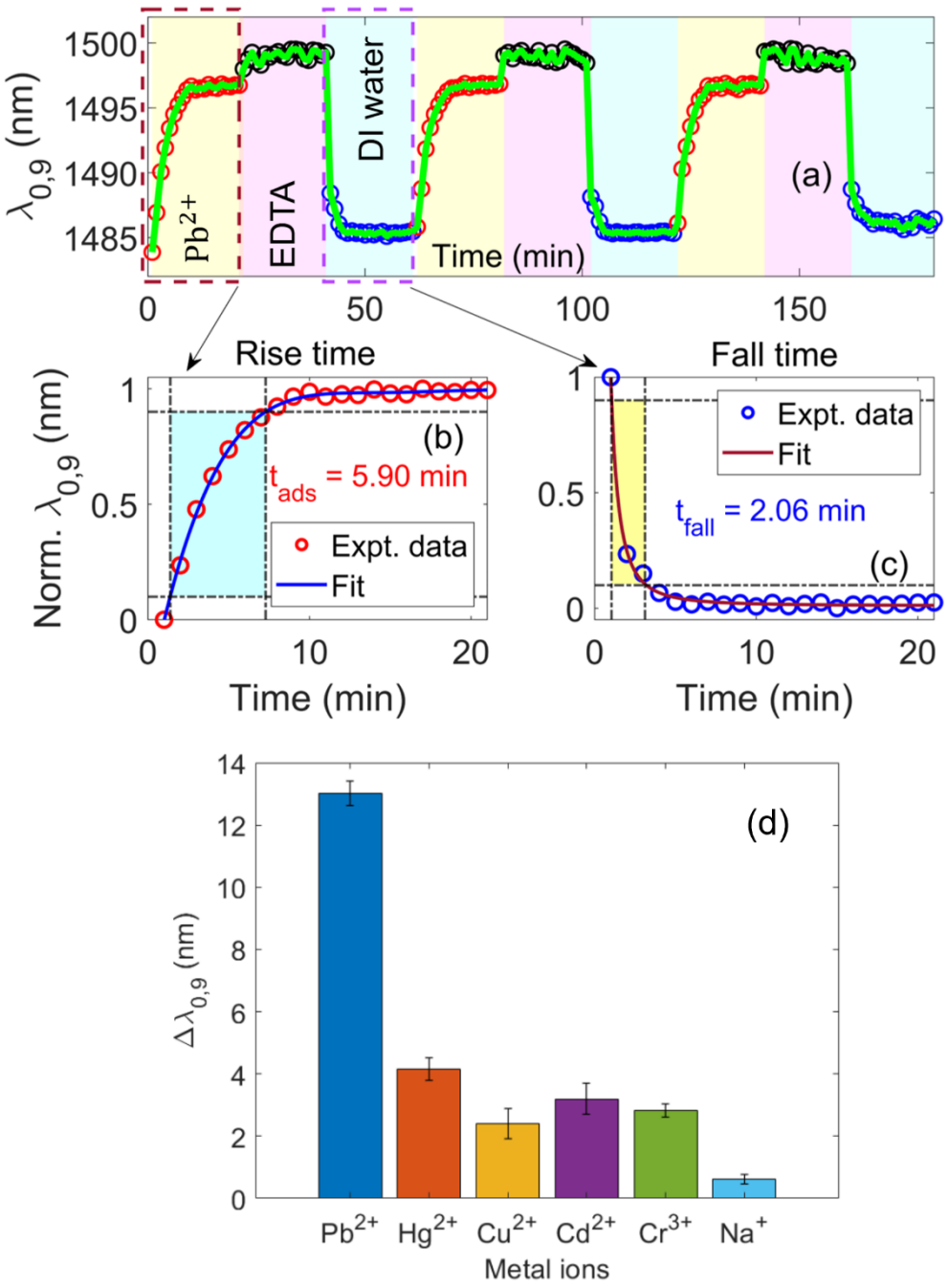

Figure 10: (a) Dynamic response of the fiber-optic lead ion sensor over three successive cycles of adsorption and desorption. The effective adsorption time (t_{ads}) of the sensor was evaluated from the plot (b) as t_{ads} = 5.90 min. Plot (c) shows the desorption fall time during DI water wash. The effective desorption time (t_{des}) was obtained as $t_{des} = t_{EDTA} + |t_{90} \sim t_{10}|_{fall}$ = 22.06 min. The metal ion desorption process was slower than the adsorption. (d) Adsorption specificity of the (CCS-NGO/PAA)$_2$ coated fiber-optic sensor. The sensor was tested with different heavy metal (Pb^{2+}, Hg^{2+}, Cu^{2+}, Cd^{2+}, Cr^{3+}, Na^{+}) ion solutions of the same 5 nM concentration.